

KeDuSR: Real-World Dual-Lens Super-Resolution via Kernel-Free Matching

Huanjing Yue¹, Zifan Cui¹, Kun Li², Jingyu Yang^{1*}

¹School of Electrical and Information Engineering, Tianjin University, China

²College of Intelligence and Computing, Tianjin University, China
{huanjing.yue, cuizifan, lik, yjy}@tju.edu.cn

Abstract

Dual-lens super-resolution (SR) is a practical scenario for reference (Ref) based SR by utilizing the telephoto image (Ref) to assist the super-resolution of the low-resolution wide-angle image (LR input). Different from general RefSR, the Ref in dual-lens SR only covers the overlapped field of view (FoV) area. However, current dual-lens SR methods rarely utilize these specific characteristics and directly perform dense matching between the LR input and Ref. Due to the resolution gap between LR and Ref, the matching may miss the best-matched candidate and destroy the consistent structures in the overlapped FoV area. Different from them, we propose to first align the Ref with the center region (namely the overlapped FoV area) of the LR input by combining global warping and local warping to make the aligned Ref be sharp and consistent. Then, we formulate the aligned Ref and LR center as value-key pairs, and the corner region of the LR is formulated as queries. In this way, we propose a kernel-free matching strategy by matching between the LR-corner (query) and LR-center (key) regions, and the corresponding aligned Ref (value) can be warped to the corner region of the target. Our kernel-free matching strategy avoids the resolution gap between LR and Ref, which makes our network have better generalization ability. In addition, we construct a DuSR-Real dataset with (LR, Ref, HR) triples, where the LR and HR are well aligned. Experiments on three datasets demonstrate that our method outperforms the second-best method by a large margin. *Our code and dataset are available at <https://github.com/ZifanCui/KeDuSR>.*

Introduction

Single Image Super-Resolution (SISR) (Liang et al. 2021; Yang, Liu, and Yang 2023) aims to reconstruct a high-resolution (HR) image from a low-resolution (LR) input, which is challenging due to the limited available information. In contrast, Reference-based SR (RefSR) introduces a similar high-resolution reference image (Ref) to assist the reconstruction process and has achieved better results. However, the development of RefSR is constrained since obtaining similar Ref for a given LR in real scenarios is difficult.

Fortunately, modern smartphones are equipped with multiple cameras of different fields of view (FoV), where the

wide-angle lens sacrifices resolution to increase the FoV, while the telephoto lens has a smaller FoV but higher resolution. Therefore, dual-lens (or dual-camera) SR is proposed (Wang et al. 2021), where the telephoto camera serves as the reference to super-resolve the wide-angle camera by transferring the matched reference details to the LR, as shown in Fig. 1. However, only the center region (namely the overlapped FoV area) of the LR image has reference content, with differences in viewpoints and colors. Meanwhile, it is difficult for the corner region¹ of the LR image to find similar contents from the reference due to the large resolution gap (as shown in Fig. 1) between the telephoto and wide-angle cameras. Therefore, the key question for real dual-lens SR is how to improve the matching and warping performance between LR and Ref when they have large resolution gaps and different FoV?

The matching problem has been widely explored in RefSR and dual-lens SR. Previous RefSR methods (Yang et al. 2020; Lu et al. 2021; Jiang et al. 2021) are conducted with synthesized LR (namely the down-sampled version of the HR) images from CUFED5 dataset, and the matching is conducted between HR \downarrow (namely LR) and Ref \downarrow (or Ref). However, when the HR and Ref are captured with different focal lengths, the resolution gap still exists. Similarly, DCSR (Wang et al. 2021) also utilizes synthesized pairs, namely that the original LR and the reference image are downsampled to generate the training triples, namely {LR \downarrow , Ref \downarrow , LR}, where the original LR serves as the ground truth. The matching is conducted between LR \downarrow and Ref \downarrow . However, the simple downsampling operation cannot simulate the resolution gap between LR and Ref since they are captured by different focal lengths, as shown in Fig. 1. SelfDZSR (Zhang et al. 2022b) directly performs matching between Ref and auxiliary-LR features, which also did not pay attention to the resolution gap. Different from them, we did not perform matching between the features of Ref \downarrow and LR. We propose a kernel-free matching strategy by matching between LR-corner and LR-center features, which perfectly avoids the resolution gap problem. In this way, our method also has a good generalization ability.

*Corresponding author.

¹We divide the LR image into two parts, where the overlapped FoV region is named as the center region and the remaining regions in the LR are named as corner region.

The warping strategy is the second key problem for dual-lens SR. General RefSR, such as (Yang et al. 2020; Huang et al. 2022) performs globally pixel-wise or patch-wise dense matching since the corresponding matched content may locate in any position in the reference and then utilize the matched index for Ref warping. The benchmark dual-lens SR work DCSR (Wang et al. 2021) also utilizes this strategy. However, for dual-lens SR, the center region of the LR has the same scene as that of the reference. Directly performing dense patch matching between the LR and Ref may miss the best-matched patch for the center region due to the large resolution gap between the LR and Ref and the matching index may be incongruent. Therefore, SelfDZSR (Zhang et al. 2022b) proposes to paste the Ref back to the center area of the warped Ref features. However, the LR center and Ref are not pixel-wise aligned and this operation introduces misalignments between the center and corner regions in the SR result. Different from them, we propose a novel center warping strategy to find the matched content for the center region, which jointly utilizes global warping and local warping. For the corner region, we utilize the kernel-free matching index for corner warping, leading to a well-aligned reference in both corner and center regions.

The third problem is how to adapt to real captured LR images in dual-lens SR? Since there is no pairwise real dual-lens SR dataset, DCSR (Wang et al. 2021) is trained with a synthesized dataset. It adapts the network to real images by finetuning with self-supervised loss. However, the finetuning strategy cannot solve the domain gap problem between synthesized and real captured ones. In contrast, SelfDZSR (Zhang et al. 2022b) proposes a self-supervised learning strategy, which utilizes the warped telephoto image as the ground truth (GT) and the center region of it serves as the reference. It introduces an auxiliary LR to make the warped LR and Ref aligned with GT during training. This makes the network pay more attention to the alignment process other than detail generation.

Recently, ZeDuSR (Xu, Yao, and Xiong 2023) proposes zero-shot learning to deal with real captured LR images by training with center region pairs, but it requires a long inference time due to online learning. Different from them, we argue that a well-aligned dual-lens SR dataset is required to further boost the real dual-lens SR performance. Therefore, we construct the first well-aligned DuSR-Real dataset, where the HR is aligned with the real captured LR and the reference is also real captured. The LR and Ref have overlapped FoV regions. In addition, we reorganize the previous dual-lens SR datasets and construct another two real datasets, namely RealMCVSR-Real and CamereFusion-Real, for comprehensively evaluation.

In summary, our contributions are as follows.

- We are the first to explore the real dual-lens SR problem via supervised learning. We propose a center warping and corner warping strategy to align the reference with the LR input, which greatly improves the alignment quality.
- We propose a kernel-free matching strategy by matching between LR-center and LR-corner, which avoids the resolution gap between the LR and Ref and makes the result

be consistent across the whole image.

- We constructed the first well-aligned DuSR-Real dataset. Extensive experiments on three datasets demonstrate the superiority of the proposed method. In addition, our method has the best generalization ability.

Related Work

Reference-Based SR

RefSR, which leverages an HR reference to improve the SR performance, is a classical topic. From traditional methods to deep learning-based methods, the RefSR performance has been greatly improved. The key problem in RefSR is matching and warping. To improve the matching and warping performance, many sophisticated methods have been proposed, such as dense patch matching based (Yue et al. 2013; Zheng et al. 2017; Zhang et al. 2019b; Yang et al. 2020), optical-flow based warping (Zheng et al. 2018), and dense matching assisted DCN (deformable convolution network) warping, such as (Shim, Park, and Kweon 2020; Jiang et al. 2021; Huang et al. 2022). Specifically, C2-matching (Jiang et al. 2021) utilized contrastive learning to overcome scale and rotation transformation gaps and employed a teacher-student correlation distillation network to address the resolution gap. To accelerate the matching process, MASA (Lu et al. 2021) and AMSA (Xia et al. 2022) explore efficient matching via a coarse-to-fine matching approach. Besides matching, advanced training and strategies are also emerging. RRSR (Zhang et al. 2022a) proposed a novel reciprocal training strategy. DATSR (Cao et al. 2022) incorporated transformer into RefSR and have achieved SOTA performance. However, all these methods perform matching between LR and Ref. Different from them, we propose a kernel-free matching strategy tailored for dual-lens SR, by matching between LR-corner and LR-center regions, which avoids the resolution gap between the LR and Ref.

Dual-Lens SR

Compared with RefSR, dual-lens SR is more practical since the telephoto camera can directly serve as the reference for the wide-angle camera. DCSR (Wang et al. 2021) was the pioneer in introducing the dual-lens SR task. Since the training was conducted with a synthesized dataset, they further proposed a self-supervised domain adaptation strategy to generalize to real-world images. To enhance matching robustness, Zou *et al.* (2023) introduced geometric constraints to make the matching results be smooth. To adapt to real images, SelfDZSR (Zhang et al. 2022b) proposed a self-supervised learning framework that directly utilized weakly aligned real-world pairs for training. ZeDuSR (Xu, Yao, and Xiong 2023) proposed a zero-shot learning strategy by training with the pairs inside the overlapped FoV region, which had a good generalization ability. RefVSR (Lee et al. 2022) and ERVSR (Kim et al. 2023) extended the dual-lens SR strategy to video SR. Unlike them, we jointly utilize center and corner warping to improve the alignment performance between LR and Ref.

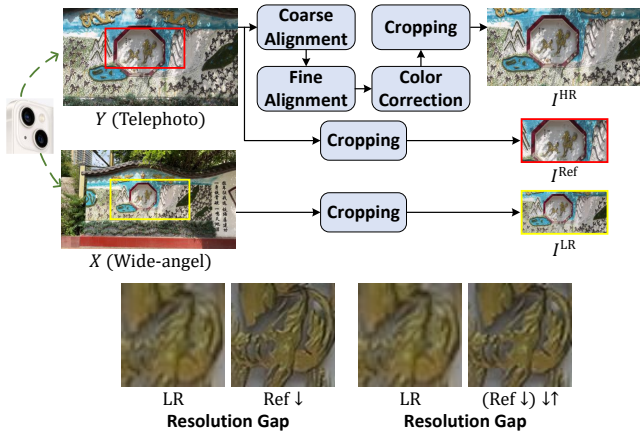


Figure 1: Illustration of our DuSR-Real dataset construction process and the resolution gap between LR and Ref.

Real-World SR Datasets

The quality of the dataset is an important factor in promoting network development and improving SR performance. The widely used SR datasets are usually constructed by downsampling the GT, thus resulting in well-aligned LR-HR pairs, such as the SISR datasets, i.e., DIV2K (Timofte et al. 2017) and the RefSR dataset CUFED5 (Zhang et al. 2019b). However, the models trained on the synthesized dataset cannot generalize well to real degraded images. Therefore, many real-world SR datasets are collected by capturing with different focuses, such as City100 (Chen et al. 2019), SR-Raw (Zhang et al. 2019a), DRealSR (Wei et al. 2020), which have greatly improved the model’s ability in dealing with real captured LR images. However, these datasets cannot be directly utilized for dual-lens SR due to the lack of triples (LR, Ref, and HR). The benchmark dual-lens SR datasets, i.e., CameraFusion (Wang et al. 2021) and RealMCVSR (Lee et al. 2022), construct the training triples by downsampling the LR and Ref, generating $\{LR\downarrow, Ref\downarrow, LR\}$, where the original LR image serves as the GT. To deal with real LR images, SelfDZSR (Zhang et al. 2022b) proposes to use the misaligned triples for training, which requires tedious operations to deal with the misalignment problem. Afterward, ZeDuSR (Xu, Yao, and Xiong 2023) explores zero-shot learning to solve the real dual-lens SR. Different from them, we argue that a real triple dataset is still needed to further boost the development of real-world dual-lens SR. Therefore, we construct a DuSR-Real dataset with well-aligned LR and HR pairs and corresponding assisted HR references with overlapped FoV.

DuSR-Real Dataset Construction

In the literature, there are two datasets, i.e., CameraFusion (Wang et al. 2021) and RealMCVSR (Lee et al. 2022) for dual-lens SR. However, they only provide LR and Ref pairs, without HR ground truth for the LR. In this work, we construct real triples for dual-lens SR.

Data Collection. The scene numbers in CameraFusion and RealMCVSR are relatively small. Therefore, we collect

a new large dataset for real dual-lens SR. Specifically, we use an iPhone 13 to capture dual-lens images through the DoubleTake App². The focal length of the telephoto lens is two times that of the wide-angle lens. Note that, different from CameraFusion (Wang et al. 2021), which utilizes lens switching to capture the same scene, we simultaneously activate both lenses for capturing. In this way, our dataset can avoid the misalignments between the two cameras in dynamic scenes and is consistent with real applications.

Data Processing. For supervised learning, we need to generate the HR GT for the input LR. We propose to warp the telephoto image with the wide-angle image to generate the HR GT and the original center area of the telephoto image can serve as the Ref. We adopt the coarse-to-fine alignment strategy proposed in (Yue, Zhang, and Yang 2022) to create well-aligned LR-HR pairs. As depicted in Fig. 1, X and Y represent the original images captured by the wide-angle lens and telephoto lens, respectively. Firstly, we employ SIFT (Lowe 2004) and RANSAC (Fischler and Bolles 1981) to calculate the optimal homography matrix to coarsely align Y with X . Then, we adopt Deepflow (Weinzaepfel et al. 2013) for fine alignment. In this work, we focus on the SR task and the color differences between LR and HR will affect the learning process. Therefore, we further utilize color correction, namely a linear scaling coefficient for each channel (Yue, Zhang, and Yang 2022), to make them have similar colors. Then, we crop the overlapped area between X and warped Y , generating the LR-HR pair I^{LR} and I^{HR} . Then, we further crop the central area (according to the relative position between the two lenses) of Y , generating I^{Ref} to serve as the reference. We totally captured 730 pairs, and manually removed 255 triples with alignment errors. Among the remaining triples (I^{LR}, I^{Ref}, I^{HR}), 420 triples are used for training, and 55 triples are used for testing.

In order to perform cross-dataset evaluation, we further apply the same processing approach on the CameraFusion (Wang et al. 2021) and RealMCVSR (Lee et al. 2022) datasets, to generate well-aligned real LR-HR pairs and the pairs that cannot be well aligned are removed. The reorganized datasets are named CameraFusion-Real and RealMCVSR-Real, respectively. Detailed information about the three datasets is provided in our supp. file.

Method

Framework Overview

Dual-lens SR is different from general RefSR since the Ref in dual-lens SR shares the same scene with that of the LR center. Therefore, we propose to deal with the center and corner region differently. As shown in Fig. 3, the Ref image first goes through center warping, and then with the index obtained from kernel-free matching, we further perform corner warping on the Ref. Combining the warped reference feature and the LR feature via an adaptive fusion module and reconstruction module, we obtain the final result I^{SR} . The following gives details about these modules in our Kernel-free matching based Dual-lens SR (termed as KeDuSR).

²<https://apps.apple.com/us/app/doubletake-by-filmic-pro/id1478041592>

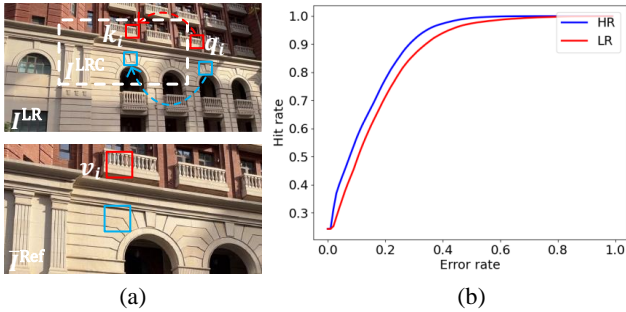


Figure 2: Illustration of the similarity between the corner and center regions, where (a) shows the similar patch pairs and (b) is the matching curve. The LR-center region is circled by a white dotted box and I^{Ref} is its corresponding HR Ref.

Center Warping

Given the LR image I^{LR} and its reference I^{Ref} , we need to first identify the overlapped area between them. Specifically, we utilize SIFT (Lowe 2004) matching to find the matched points between I^{Ref} and I^{LR} . Then, we utilize RANSAC (Fischler and Bolles 1981) to filter outliers, and use the inliers to calculate the homography matrix, which is applied on I^{Ref} and generates the warped reference \bar{I}^{Ref} . Afterward, we crop the area in I^{LR} that corresponds to \bar{I}^{Ref} , and name it as the center region of the LR, denoted as I^{LRC} . After this global warping, \bar{I}^{Ref} is coarsely aligned with I^{LRC} .

However, there are still small displacements between \bar{I}^{Ref} and I^{LRC} , which may cause alignment errors in the following corner warping. Therefore, we further utilize the faster and differentiable flow-guided DCN (Chan et al. 2022) for local warping. Note that, we did not utilize DeepFlow for center warping since it is much slower and nondifferentiable. To reduce the computation cost, we downsample \bar{I}^{Ref} to make it have the same scale as that of I^{LRC} . Then, we utilize the pre-trained Spynet (Ranjan and Black 2017) to compute the optical flow f between $\bar{I}^{\text{Ref}}_{\downarrow}$ and I^{LRC} . Then, we utilize residual blocks (ResBlocks) to extract features from I^{LRC} and \bar{I}^{Ref} , generating F^{LRC} and \bar{F}^{Ref} . Afterwards, the upsampled optical flow f_{\uparrow} is utilized to guide DCN (Dai et al. 2017; Zhu et al. 2019) to align \bar{F}^{Ref} with F^{LRC} , generating the fine-aligned features \hat{F}^{Ref} .

Note that, compared with the widely used dense patch matching-based warping, our global warping and local warping combined strategy can preserve the reference image structures, which not only improves the following corner-warping performance but also improves the final SR quality in the center region.

Kernel-Free Matching and Corner Warping

An intuitive strategy for warping the corner region is performing patch matching between the corner of I^{LR} and the reference I^{Ref} . However, there is a large resolution gap between them. Even after downsampling, the resolution gap still exists between I^{LR} and $I^{\text{Ref}}_{\downarrow\downarrow\uparrow}$ (as shown in Fig. 1) since simple downsampling cannot simulate the mapping

between the two cameras. Another strategy is learning the mapping process via KernelGAN (Bell-Kligler, Shocher, and Irani 2019) or probabilistic degradation model (PDM) (Luo et al. 2022), and utilizing the learned kernel to degrade I^{Ref} . However, the kernel depends on cameras, which makes the kernel learned with one specific camera does not generalize well to other cameras.

In contrast, we observe that due to the nonlocal similarity, for one query patch (q_i) in the corner region, we can find its similar patch (k_i) in the center region, as shown in Fig. 2 (a). To visualize the similarity between corner region and center region, we plot the matching curve, namely hit rate versus error rate in Fig. 2 (b). The error rate is defined as $e_r = \|q - k\|_2 / \|q\|_2$, where k is the matched patch from the center region with the minimal mean square error for q . The hit rate is the percentage of the query patch whose error rate is smaller than e_r . The blue matching curve is obtained by matching between the HR query and the HR key, but the e_r is obtained by the HR patches with the corresponding index. For more than 90% of patches, their error rates are smaller than 0.3, which indicates a high similarity between corner and center regions. In addition, the matching in LR domain can well approximate the matching in HR domain. Therefore, in this work, we propose to perform matching between the corner and center regions of the LR image. Since this matching process is not influenced by different camera kernels, we formulate it as kernel-free matching.

Following (Yang et al. 2020; Wang et al. 2021), we also perform matching in the VGG (denoted as ϕ) feature space by extracting features from I^{LR} and I^{LRC} . The features are densely divided into 3×3 patches with a stride of 1, and the cosine similarity $S_{i,j}$ is computed between each patch pair, namely P_i^{LR} and P_j^{LRC} . For P_i^{LR} , its matched patch is the one that has the highest similarity score, and the matched index M_i and confidence score C_i can be obtained by

$$M_i = \arg \max_j S_{i,j}, C_i = \max_j S_{i,j}. \quad (1)$$

Then, we utilize the matched index map to extract HR matched patches from the Ref. Therefore, the reference warping result for the corner region is

$$\tilde{F}_{2i}^{\text{Ref}} = \hat{F}_{M_i}^{\text{Ref}}, \quad (2)$$

where \tilde{F}_i^{Ref} denotes the patch value of \hat{F}^{Ref} in the i^{th} patch position. Since the query patches are densely extracted, the overlapped value patches are averaged in the overlapped region. In addition, the center region of \hat{F}^{Ref} is indeed the center warping result \hat{F}^{Ref} . Correspondingly, the center region of the confidence map is set to 1.

SISR Encoder

As demonstrated in (Huang et al. 2022), coupling the image super-resolution task from the input LR image with the texture transfer task from the reference will introduce interference. Therefore we also decouple the SISR task into a separate module, which is constructed by 24 residual blocks with channel attention. The extracted features are upsampled (named as F^{LR}) to cope with the size of the aligned reference feature. Note that, different from the two-stage training

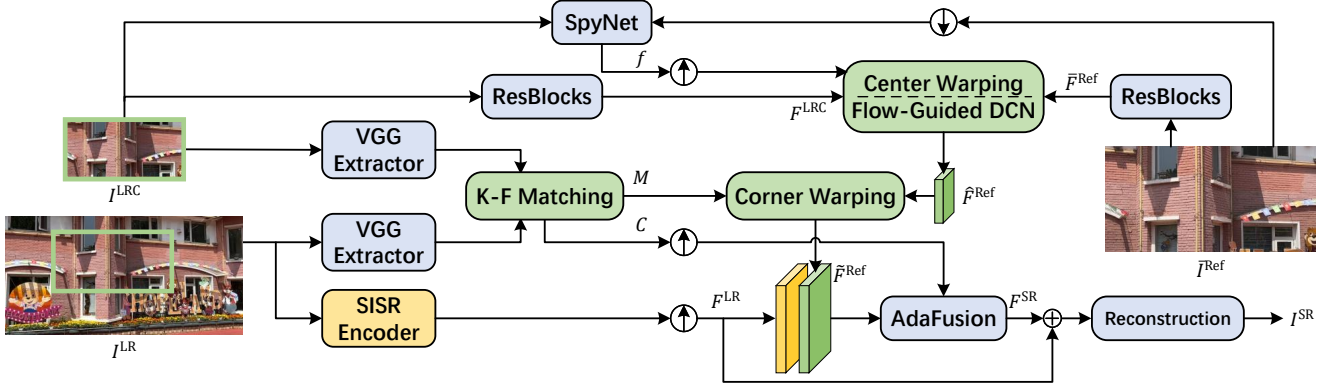


Figure 3: The framework of our KeDuSR. Kernel-Free Matching is performed between LR-corner and LR-center(I^{LRC}) to obtain the index map M and confidence map C . Then, employing center warping and corner warping, we obtain the warped high-resolution feature map \tilde{F}^{Ref} of the reference. After fusion with F^{LR} , we generate the SR result I^{SR} .

approach used in (Huang et al. 2022), we train our SISR encoder as an integral part of the entire network.

Adaptive Fusion

The warped reference feature \tilde{F}^{Ref} and LR image feature F^{LR} are complementary to each other, and we utilize a fusion model to fuse them together. Since the matching quality for different positions is different, inspired by (Wang et al. 2021), we also utilize adaptive fusion by introducing the confidence map obtained in the matching process. In addition, instead of fusing \tilde{F}^{Ref} , we fuse its high-frequency part $\tilde{F}_{hf}^{Ref} = \tilde{F}^{Ref} - \tilde{F}^{Ref} \downarrow \uparrow$. This process is formulated as

$$F^{SR} = \Phi(\text{concat}(g(C) \cdot \tilde{F}_{hf}^{Ref}, F^{LR})), \quad (3)$$

where C denotes the confidence map, $g(\cdot)$ represents the convolution operations, \cdot represents the element-wise multiplication, and Φ represent the AdaFusion block. The AdaFusion module is constructed by ResBlocks with spatial and channel attention.

Loss Functions

Following previous RefSR methods, we also utilize hybrid loss functions. First, for reconstruction loss, we utilize Charbonnier loss (Lai et al. 2017), which is a differentiable variant of ℓ_1 loss, denoted as

$$\mathcal{L}_{ch} = \sqrt{\|I^{HR} - I^{SR}\|_2^2} + \varepsilon, \quad (4)$$

where $\varepsilon = 1 \times 10^{-6}$. I^{HR} denotes the HR GT, while I^{SR} denotes the SR result. For better visual effects, we further incorporate perceptual loss and adversarial loss. The perceptual loss is expressed as

$$\mathcal{L}_{per} = \|\phi_i(I^{HR}) - \phi_i(I^{SR})\|_2, \quad (5)$$

where ϕ_i denotes the i -th layer of VGG19. We adopt the Relativistic GANs (Jolicoeur-Martineau 2018) as our adversarial loss (Goodfellow et al. 2014), denoted as \mathcal{L}_{adv} . In summary, our hybrid loss can be represented as

$$\mathcal{L} = \mathcal{L}_{ch} + \lambda_1 \mathcal{L}_{per} + \lambda_2 \mathcal{L}_{adv}, \quad (6)$$

where the weighting parameters λ_1 and λ_2 are set to 1×10^{-3} and 1×10^{-4} , respectively. Note that, we provide two results in experiments. One is trained with only the reconstruction loss \mathcal{L}_{ch} and the other is trained with the hybrid loss \mathcal{L} .

Experiments

Training Details and Datasets

During training, the batch size is 4, and the patch size for the input LR is 128×128 . We utilized the Adam optimizer (Kingma and Ba 2014) and the cosine annealing scheme (Loshchilov and Hutter 2016). The learning rate is initially set to 10^{-4} and is decayed to 10^{-6} . All experiments were conducted using PyTorch (Paszke et al. 2019) on an Nvidia GeForce RTX 3090 GPU.

We conduct comparisons on three datasets, namely our DuSR-Real, the reorganized CameraFusion-Real, and RealMCVSR-Real datasets. Our DuSR-Real contains 420 training triples and 55 testing images, and the HR GT has a resolution of 1792×896 . The RealMCVSR-Real (CameraFusion-Real) consists of 330 (83) training triples and 50 (15) testing images, and the GT has a resolution of 1792×896 (3584×2560).

Comparison with State-of-the-arts

To evaluate the effectiveness of our KeDuSR, we compare with three kinds of SR methods, including the SISR methods: RCAN (Zhang et al. 2018b), SwinIR (Liang et al. 2021), ESRGAN (Wang et al. 2018), BSRGAN (Zhang et al. 2021), the RefSR methods: TTSR (Yang et al. 2020), MASA (Lu et al. 2021), DASTR (Cao et al. 2022), and the dual-lens SR methods: DCSR (Wang et al. 2021), SelfDZSR (Zhang et al. 2022b), ZeDuSR (Xu, Yao, and Xiong 2023). For a fair comparison, we retrained the aforementioned methods with the same training set as that used in our method. SISR methods use the LR-HR pair during training, while RefSR methods use the LR-Ref-HR triples (except for ZeDuSR, which uses LR-Ref pairs). For SelfDZSR, since the Ref and LR have large and irregular displacements in our

Method	Latency (s)	Full-Image	Center-Image	Corner-Image
		PSNR \uparrow /SSIM \uparrow /LPIPS \downarrow	PSNR/SSIM	PSNR/SSIM
RCAN- ℓ	0.69	26.44 / 0.8676 / 0.147	26.91 / 0.8704	26.33 / 0.8667
SwinIR- ℓ	2.85	26.14 / 0.8601 / 0.157	26.35 / 0.8612	26.11 / 0.8597
ESRGAN	0.08	25.78 / 0.8622 / 0.152	25.91 / 0.8637	25.77 / 0.8617
BSRGAN	0.45	24.77 / 0.8227 / 0.202	25.01 / 0.8233	24.71 / 0.8225
TTSR- ℓ	7.51	26.48 / 0.8676 / 0.147	27.69 / 0.8810	26.17 / 0.8631
MASA- ℓ	1.52	26.36 / 0.8592 / 0.160	26.85 / 0.8620	26.25 / 0.8582
DATSR- ℓ	9.35	26.17 / 0.8583 / 0.157	26.48 / 0.8596	26.11 / 0.8579
DCSR- ℓ	0.84	<u>26.77 / 0.8748 / 0.134</u>	<u>28.87 / 0.9078</u>	26.29 / 0.8635
DCSR	0.84	26.19 / 0.8553 / 0.110	28.05 / 0.8929	25.75 / 0.8425
SelfDZSR- ℓ	0.17	26.27 / 0.8559 / 0.158	26.97 / 0.8591	26.10 / 0.8548
SelfDZSR	0.17	25.98 / 0.8455 / 0.105	26.61 / 0.8496	25.81 / 0.8442
ZeDuSR- ℓ	180.0	25.41 / 0.8247 / 0.191	26.29 / 0.8336	25.21 / 0.8216
KeDuSR- ℓ	0.51	27.66 / 0.8890 / 0.117	29.58 / 0.9303	27.24 / 0.8750
KeDuSR	0.51	27.18 / 0.8752 / 0.084	29.06 / 0.9219	26.77 / 0.8593

Table 1: Quantitative comparisons on DuSR-Real. Bold and underlined indicate the best and second-best performance, respectively. ℓ denotes training with only reconstruction loss. Latency indicates the time required to generate one HR result (1792×896) using one NVIDIA 3090 GPU.

Method	Full-Image	Center-Image	Corner-Image
	PSNR \uparrow /SSIM \uparrow /LPIPS \downarrow	PSNR/SSIM	PSNR/SSIM
RCAN- ℓ	25.96 / 0.8033 / 0.234	25.69 / 0.7937	26.12 / 0.8065
SwinIR- ℓ	25.78 / 0.7982 / 0.246	25.50 / 0.7885	25.94 / 0.8015
TTSR- ℓ	25.92 / 0.8017 / 0.235	25.94 / 0.7962	25.98 / 0.8036
MASA- ℓ	25.95 / 0.7989 / 0.239	25.81 / 0.7899	26.07 / 0.8020
DATSR- ℓ	25.81 / 0.7975 / 0.242	25.58 / 0.7882	25.95 / 0.8007
DCSR- ℓ	<u>26.28 / 0.8111 / 0.217</u>	<u>27.19 / 0.8298</u>	26.08 / 0.8048
DCSR	25.85 / 0.7966 / 0.186	26.98 / 0.8476	25.58 / 0.7793
SelfDZSR- ℓ	25.33 / 0.7928 / 0.246	25.66 / 0.7860	25.30 / 0.7952
SelfDZSR	25.24 / 0.7786 / <u>0.175</u>	25.50 / 0.7732	25.23 / 0.7805
ZeDuSR- ℓ	24.98 / 0.7702 / 0.262	25.38 / 0.7650	24.93 / 0.7720
KeDuSR- ℓ	27.05 / 0.8406 / 0.180	29.25 / 0.9191	26.56 / 0.8139
KeDuSR	26.42 / 0.8184 / 0.127	28.51 / 0.9090	25.95 / 0.7875

Table 2: Quantitative comparisons on RealMCVSR-Real.

dataset, we did not paste the center Ref back to its warped features to avoid misalignment artifacts.

Quantitative Comparison. We evaluate all the methods on three datasets, as shown in Tables 1, 2, 3. Full-image results represent the quantitative results of the entire image, the center-image corresponds to the results in overlapped FoV area, and the corner-image represents excluding the center-image from the full-image. For the models trained with only reconstruction loss, we denote it with ℓ . Otherwise, the corresponding model is trained with hybrid loss functions as proposed in their paper.

On all three datasets, our method outperforms the second-best method by a large margin in terms of PSNR, SSIM (2004), and LPIPS (2018a). In addition, our method achieves the best performance in both the center and corner regions. For TTSR, its center result is better than that of RCAN due to the introduction of HR Ref. However, its corner result is worse since it cannot utilize Ref patches well. Meanwhile, DCSR works much better in the center region than TTSR due to its robust feature warping and fusion strategy. Different from them, we utilize a tailored center warping and kernel-free matching based corner warping, which greatly improves the matching performance in both center and corner regions. Meanwhile, the zero-shot learning (ZeDuSR) method can only utilize the single image information. Therefore, their performance is also inferior to ours.

Method	Full-Image	Center-Image	Corner-Image
	PSNR \uparrow /SSIM \uparrow /LPIPS \downarrow	PSNR/SSIM	PSNR/SSIM
RCAN- ℓ	25.67 / 0.8049 / 0.308	26.65 / 0.8158	25.45 / 0.8012
SwinIR- ℓ	25.32 / 0.8007 / 0.315	25.81 / 0.8073	25.22 / 0.7985
TTSR- ℓ	25.83 / 0.8044 / 0.311	26.75 / 0.8188	25.62 / 0.7996
MASA- ℓ	25.78 / 0.8030 / 0.303	26.70 / 0.8155	25.58 / 0.7988
DCSR- ℓ	26.02 / 0.8123 / 0.293	28.37 / 0.8440	25.51 / 0.8016
DCSR	25.47 / 0.7605 / 0.165	27.14 / 0.7883	25.08 / 0.7512
DCSR-SRA	24.75 / 0.7347 / 0.189	25.62 / 0.7626	24.55 / 0.7254
SelfDZSR- ℓ	25.94 / 0.8041 / 0.283	27.10 / 0.8148	25.68 / 0.8005
SelfDZSR	25.64 / 0.7790 / <u>0.151</u>	26.77 / 0.7897	25.39 / 0.7753
ZeDuSR- ℓ	26.16 / 0.7920 / 0.279	27.44 / 0.8067	25.87 / 0.7871
KeDuSR- ℓ	27.53 / 0.8292 / 0.276	30.48 / 0.8656	26.93 / 0.8169
KeDuSR	27.00 / 0.7931 / 0.133	29.77 / 0.8418	26.43 / 0.7768

Table 3: Quantitative comparisons on CameraFusion-Real.

Variant	Traditional Matching	Center Warping	Corner Warping	PSNR \uparrow /SSIM \uparrow
A	✓			27.03 / 0.8801
B		✓		27.16 / 0.8757
C			✓	27.50 / 0.8804
D		✓	✓	27.66 / 0.8890

Table 4: Ablation study on our key modules, evaluated on DuSR-Real dataset.

Note that, ZeDuSR works better in the CameraFusion-Real dataset since the image size in this dataset is large, which makes ZeDuSR extract more training pairs from one single image. In addition, our method ranks second among all the RefSR methods in terms of latency.

We also evaluate the benefits of training with real pairs over finetuning. We utilize the released weights of DCSR, which is finetuned by the Self-supervised Real-image Adaptation (SRA) strategy, and term it DCSR-SRA. As shown in Table 3, DCSR-SRA falls largely behind the original DCSR trained with our constructed real pairs.

Qualitative Comparison. Fig. 4 presents the visual comparison results. In the center region, our method achieves results that closely resemble the HR GT, surpassing other existing methods by a significant margin. In the corner region, our approach is capable of recovering more fine-grained details if similar textures are present in the Ref. In addition, for large LR input, the majority of methods need to divide the LR input into blocks due to the limitation of available memory. In this case, our method can avoid the blocking artifacts due to our kernel-free matching strategy while the compared methods suffer from these artifacts. More results are provided in our supp. file.

Ablation Study

We conduct ablation experiments on our proposed matching and warping strategy. First, we remove the proposed center warping and corner warping and replace them with traditional dense feature matching, namely matching between the VGG features of I^{LR} and I^{Ref} . Then utilize the matching result for reference warping. As shown in Table 4, this (variant A) degrades the result by 0.63 dB. Note that, variant A is our baseline, which is better than SOTA RefSR methods, verifying that our proposed baseline is a robust baseline

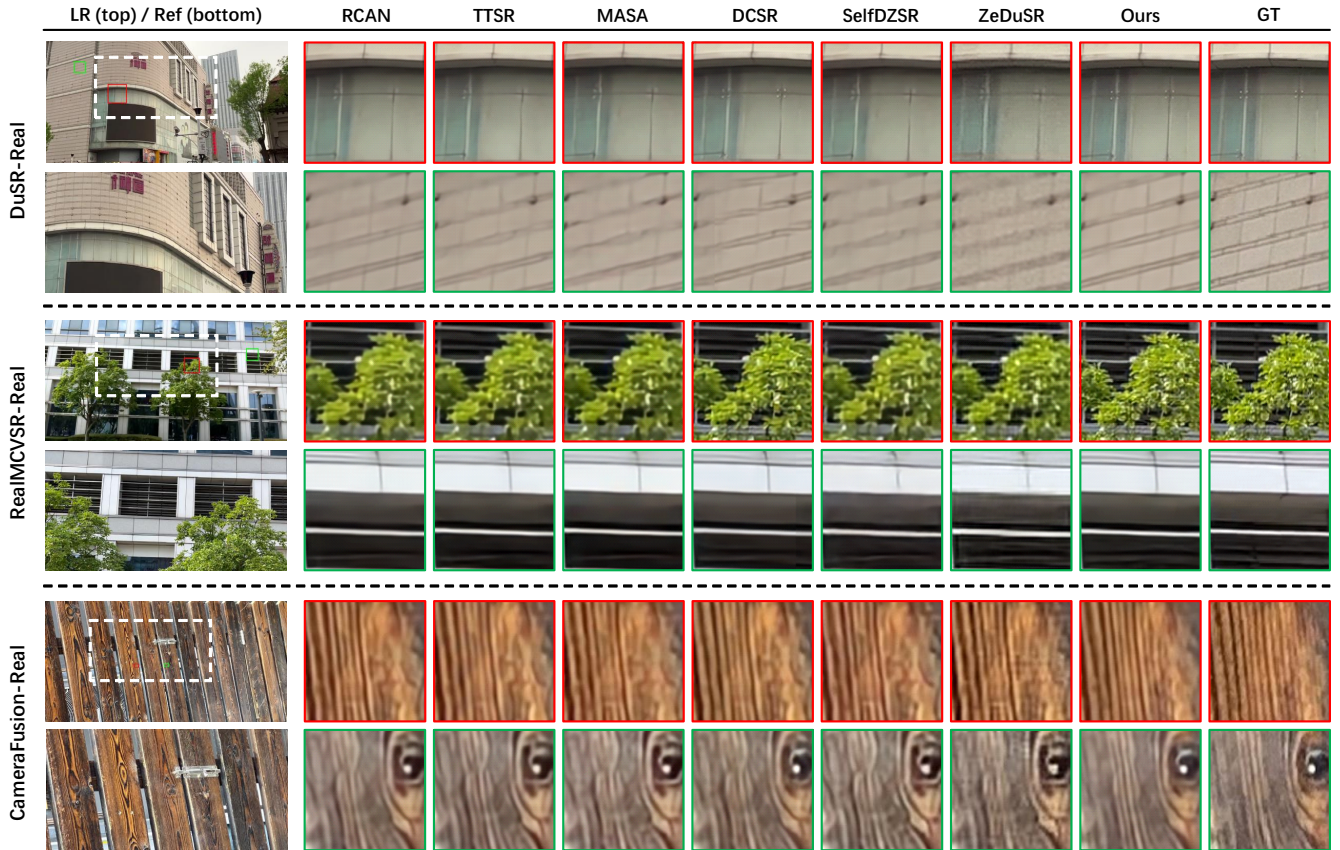


Figure 4: Visual comparisons on real-world dual-lens datasets. The white dotted box indicates the overlapped FoV area between LR and Ref. The presented results are obtained with only reconstruction loss.

for the dual-lens SR task. For variant B, we remove the corner warping process, namely that we only utilize the center warping result and there is no reference for the corner region. Variant B still outperforms variant A in terms of PSNR since the center region is well reconstructed. This demonstrates that our global and local warping combined strategy is effective for the center region. For variant C, we remove the center warping, namely that we only utilize the coarsely aligned reference feature F^{Ref} for the center region, and thus the key-value pair in kernel-free matching is not accurately aligned. Therefore, the result of variant C is worse than our full model (variant D). In summary, our center warping and corner warping are essential for improving the dual-lens SR performance.

Generalization Evaluation

We also evaluate the generalization ability of different models trained on DuSR-Real by testing on the two other datasets. As shown in Table 5, our method has the best generalization ability, even outperforming the zero-shot learning method ZeDuSR. The main reason is that our kernel-free matching strategy is independent of cameras.

Method	RealMCVSR-Real			CameraFusion-Real		
	PSNR \uparrow	SSIM \uparrow	LPIPS \downarrow	PSNR \uparrow	SSIM \uparrow	LPIPS \downarrow
TTSR- ℓ	24.67	0.7814	0.248	25.23	0.7760	0.289
MASA- ℓ	24.99	0.7830	0.258	25.45	0.7769	0.291
DCSR- ℓ	25.46	0.7986	0.226	25.58	0.7931	0.263
SelfDZSR- ℓ	24.86	0.7778	0.252	25.55	0.7805	0.285
ZeDuSR- ℓ	24.98	0.7702	0.262	26.16	0.7920	0.279
KeDuSR- ℓ	26.55	0.8325	0.186	27.24	0.8178	0.215

Table 5: Generalization evaluation with the model trained on DuSR-Real.

Conclusion

In this work, we proposed a KeDuSR network to deal with the real dual-lens SR task. We designed a global and local combined warping strategy to make the Ref well-aligned with the center region of LR input. Then, we formulate the LR center and the aligned reference as key-value pairs and propose a kernel-free matching strategy, whose matching index is used for corner warping. Afterward, we fuse the features of enhanced LR input and the features of corner and center well-aligned reference to generate the SR result. Experiments demonstrate the superiority of the proposed method. We also construct a DuSR-Real dataset with well-aligned pairs to facilitate research in this area.

Acknowledgments

This work was supported in part by the National Natural Science Foundation of China under Grant 62072331, Grant 62231018, and Grant 62171317.

References

- Bell-Kligler, S.; Shocher, A.; and Irani, M. 2019. Blind super-resolution kernel estimation using an internal-gan. *Advances in Neural Information Processing Systems*, 32.
- Cao, J.; Liang, J.; Zhang, K.; Li, Y.; Zhang, Y.; Wang, W.; and Gool, L. V. 2022. Reference-Based Image Super-Resolution with Deformable Attention Transformer. In *Computer Vision—ECCV 2022: 17th European Conference, Tel Aviv, Israel, October 23–27, 2022, Proceedings, Part XVIII*, 325–342. Springer.
- Chan, K. C.; Zhou, S.; Xu, X.; and Loy, C. C. 2022. Basicvsr++: Improving video super-resolution with enhanced propagation and alignment. In *Proceedings of the IEEE/CVF conference on computer vision and pattern recognition*, 5972–5981.
- Chen, C.; Xiong, Z.; Tian, X.; Zha, Z.-J.; and Wu, F. 2019. Camera lens super-resolution. In *Proceedings of the IEEE/CVF Conference on Computer Vision and Pattern Recognition*, 1652–1660.
- Dai, J.; Qi, H.; Xiong, Y.; Li, Y.; Zhang, G.; Hu, H.; and Wei, Y. 2017. Deformable convolutional networks. In *Proceedings of the IEEE international conference on computer vision*, 764–773.
- Fischler, M. A.; and Bolles, R. C. 1981. Random sample consensus: a paradigm for model fitting with applications to image analysis and automated cartography. *Communications of the ACM*, 24(6): 381–395.
- Goodfellow, I.; Pouget-Abadie, J.; Mirza, M.; Xu, B.; Warde-Farley, D.; Ozair, S.; Courville, A.; and Bengio, Y. 2014. Generative adversarial nets. *Advances in neural information processing systems*, 27.
- Huang, Y.; Zhang, X.; Fu, Y.; Chen, S.; Zhang, Y.; Wang, Y.-F.; and He, D. 2022. Task Decoupled Framework for Reference-based Super-Resolution. In *Proceedings of the IEEE/CVF Conference on Computer Vision and Pattern Recognition*, 5931–5940.
- Jiang, Y.; Chan, K. C.; Wang, X.; Loy, C. C.; and Liu, Z. 2021. Robust reference-based super-resolution via c2-matching. In *Proceedings of the IEEE/CVF Conference on Computer Vision and Pattern Recognition*, 2103–2112.
- Jolicoeur-Martineau, A. 2018. The relativistic discriminator: a key element missing from standard GAN. *arXiv preprint arXiv:1807.00734*.
- Kim, Y.; Lim, J.; Cho, H.; Lee, M.; Lee, D.; Yoon, K.-J.; and Choi, H.-J. 2023. Efficient Reference-based Video Super-Resolution (ERVSR): Single Reference Image Is All You Need. In *Proceedings of the IEEE/CVF Winter Conference on Applications of Computer Vision*, 1828–1837.
- Kingma, D. P.; and Ba, J. 2014. Adam: A method for stochastic optimization. *arXiv preprint arXiv:1412.6980*.
- Lai, W.-S.; Huang, J.-B.; Ahuja, N.; and Yang, M.-H. 2017. Deep laplacian pyramid networks for fast and accurate super-resolution. In *Proceedings of the IEEE conference on computer vision and pattern recognition*, 624–632.
- Lee, J.; Lee, M.; Cho, S.; and Lee, S. 2022. Reference-based video super-resolution using multi-camera video triplets. In *Proceedings of the IEEE/CVF Conference on Computer Vision and Pattern Recognition*, 17824–17833.
- Liang, J.; Cao, J.; Sun, G.; Zhang, K.; Van Gool, L.; and Timofte, R. 2021. Swinir: Image restoration using swin transformer. In *Proceedings of the IEEE/CVF international conference on computer vision*, 1833–1844.
- Loshchilov, I.; and Hutter, F. 2016. Sgdr: Stochastic gradient descent with warm restarts. *arXiv preprint arXiv:1608.03983*.
- Lowe, D. G. 2004. Distinctive image features from scale-invariant keypoints. *International journal of computer vision*, 60: 91–110.
- Lu, L.; Li, W.; Tao, X.; Lu, J.; and Jia, J. 2021. Masa-sr: Matching acceleration and spatial adaptation for reference-based image super-resolution. In *Proceedings of the IEEE/CVF Conference on Computer Vision and Pattern Recognition*, 6368–6377.
- Luo, Z.; Huang, Y.; Li, S.; Wang, L.; and Tan, T. 2022. Learning the degradation distribution for blind image super-resolution. In *Proceedings of the IEEE/CVF Conference on Computer Vision and Pattern Recognition*, 6063–6072.
- Paszke, A.; Gross, S.; Massa, F.; Lerer, A.; Bradbury, J.; Chanan, G.; Killeen, T.; Lin, Z.; Gimelshein, N.; Antiga, L.; et al. 2019. Pytorch: An imperative style, high-performance deep learning library. *Advances in neural information processing systems*, 32.
- Ranjan, A.; and Black, M. J. 2017. Optical flow estimation using a spatial pyramid network. In *Proceedings of the IEEE conference on computer vision and pattern recognition*, 4161–4170.
- Shim, G.; Park, J.; and Kweon, I. S. 2020. Robust reference-based super-resolution with similarity-aware deformable convolution. In *Proceedings of the IEEE/CVF conference on computer vision and pattern recognition*, 8425–8434.
- Timofte, R.; Agustsson, E.; Van Gool, L.; Yang, M.-H.; and Zhang, L. 2017. Ntire 2017 challenge on single image super-resolution: Methods and results. In *Proceedings of the IEEE conference on computer vision and pattern recognition workshops*, 114–125.
- Wang, T.; Xie, J.; Sun, W.; Yan, Q.; and Chen, Q. 2021. Dual-camera super-resolution with aligned attention modules. In *Proceedings of the IEEE/CVF International Conference on Computer Vision*, 2001–2010.
- Wang, X.; Yu, K.; Wu, S.; Gu, J.; Liu, Y.; Dong, C.; Qiao, Y.; and Change Loy, C. 2018. Esrgan: Enhanced super-resolution generative adversarial networks. In *Proceedings of the European conference on computer vision (ECCV) workshops*, 0–0.
- Wang, Z.; Bovik, A. C.; Sheikh, H. R.; and Simoncelli, E. P. 2004. Image quality assessment: from error visibility to

- structural similarity. *IEEE transactions on image processing*, 13(4): 600–612.
- Wei, P.; Xie, Z.; Lu, H.; Zhan, Z.; Ye, Q.; Zuo, W.; and Lin, L. 2020. Component divide-and-conquer for real-world image super-resolution. In *Computer Vision–ECCV 2020: 16th European Conference, Glasgow, UK, August 23–28, 2020, Proceedings, Part VIII 16*, 101–117. Springer.
- Weinzaepfel, P.; Revaud, J.; Harchaoui, Z.; and Schmid, C. 2013. DeepFlow: Large displacement optical flow with deep matching. In *Proceedings of the IEEE international conference on computer vision*, 1385–1392.
- Xia, B.; Tian, Y.; Hang, Y.; Yang, W.; Liao, Q.; and Zhou, J. 2022. Coarse-to-fine embedded patchmatch and multi-scale dynamic aggregation for reference-based super-resolution. In *Proceedings of the AAAI Conference on Artificial Intelligence*, 2768–2776.
- Xu, R.; Yao, M.; and Xiong, Z. 2023. Zero-Shot Dual-Lens Super-Resolution. In *Proceedings of the IEEE/CVF Conference on Computer Vision and Pattern Recognition*, 9130–9139.
- Yang, F.; Yang, H.; Fu, J.; Lu, H.; and Guo, B. 2020. Learning texture transformer network for image super-resolution. In *Proceedings of the IEEE/CVF conference on computer vision and pattern recognition*, 5791–5800.
- Yang, Q.; Liu, Y.; and Yang, J. 2023. Two-branch crisscross network for realistic and accurate image super-resolution. *Displays*, 80: 102549.
- Yue, H.; Sun, X.; Yang, J.; and Wu, F. 2013. Landmark image super-resolution by retrieving web images. *IEEE Transactions on Image Processing*, 22(12): 4865–4878.
- Yue, H.; Zhang, Z.; and Yang, J. 2022. Real-RawVSR: Real-World Raw Video Super-Resolution with a Benchmark Dataset. In *Proceedings of the European conference on computer vision (ECCV)*, 608–624.
- Zhang, K.; Liang, J.; Van Gool, L.; and Timofte, R. 2021. Designing a practical degradation model for deep blind image super-resolution. In *Proceedings of the IEEE/CVF International Conference on Computer Vision*, 4791–4800.
- Zhang, L.; Li, X.; He, D.; Li, F.; Wang, Y.; and Zhang, Z. 2022a. RRSR: Reciprocal Reference-Based Image Super-Resolution with Progressive Feature Alignment and Selection. In *Computer Vision–ECCV 2022: 17th European Conference, Tel Aviv, Israel, October 23–27, 2022, Proceedings, Part XIX*, 648–664. Springer.
- Zhang, R.; Isola, P.; Efros, A. A.; Shechtman, E.; and Wang, O. 2018a. The unreasonable effectiveness of deep features as a perceptual metric. In *Proceedings of the IEEE conference on computer vision and pattern recognition*, 586–595.
- Zhang, X.; Chen, Q.; Ng, R.; and Koltun, V. 2019a. Zoom to learn, learn to zoom. In *Proceedings of the IEEE/CVF Conference on Computer Vision and Pattern Recognition*, 3762–3770.
- Zhang, Y.; Li, K.; Li, K.; Wang, L.; Zhong, B.; and Fu, Y. 2018b. Image super-resolution using very deep residual channel attention networks. In *Proceedings of the European conference on computer vision (ECCV)*, 286–301.
- Zhang, Z.; Wang, R.; Zhang, H.; Chen, Y.; and Zuo, W. 2022b. Self-supervised Learning for Real-World Super-Resolution from Dual Zoomed Observations. In *Computer Vision–ECCV 2022: 17th European Conference, Tel Aviv, Israel, October 23–27, 2022, Proceedings, Part XVIII*, 610–627. Springer.
- Zhang, Z.; Wang, Z.; Lin, Z.; and Qi, H. 2019b. Image super-resolution by neural texture transfer. In *Proceedings of the IEEE/CVF conference on computer vision and pattern recognition*, 7982–7991.
- Zheng, H.; Ji, M.; Han, L.; Xu, Z.; Wang, H.; Liu, Y.; and Fang, L. 2017. Learning Cross-scale Correspondence and Patch-based Synthesis for Reference-based Super-Resolution. In *BMVC*, volume 1, 2.
- Zheng, H.; Ji, M.; Wang, H.; Liu, Y.; and Fang, L. 2018. Crossnet: An end-to-end reference-based super resolution network using cross-scale warping. In *Proceedings of the European conference on computer vision (ECCV)*, 88–104.
- Zhu, X.; Hu, H.; Lin, S.; and Dai, J. 2019. Deformable convnets v2: More deformable, better results. In *Proceedings of the IEEE/CVF conference on computer vision and pattern recognition*, 9308–9316.
- Zou, H.; Xu, L.; and Okatani, T. 2023. Geometry Enhanced Reference-Based Image Super-Resolution. In *Proceedings of the IEEE/CVF Conference on Computer Vision and Pattern Recognition*, 6123–6132.

Supplementary File

Real Dual-Lens Datasets

The original RealMCVSR (Lee et al. 2022) dataset contains 161 sets of triples with ultra-wide, wide-angle, and telephoto videos, which can be used for $2\times$ and $4\times$ super-resolution with synthesized downsampling. Different from the original settings, we extract frames from the ultra-wide (LR) and wide-angle (HR and Ref) videos for $2\times$ real-world image SR. To avoid repetitive content, for each video, we extract two or three frames. Then, we apply our alignment method (as mentioned in Fig. 1 of the main paper) on the extracted frames to construct LR-HR-Ref triples. After removing the LR-HR pairs with large misalignments, we construct the RealMCVSR-Real dataset, which contains 330 frames from 210 scenes. However, the scene number is still fewer than previous image SR datasets. Note that, the original RealMCVSR was captured with motion blur and the LR input is heavily degraded compared with the HR. In other words, the resolution gap between LR and Ref in this dataset is larger. Thanks to our kernel-free matching, our method has the best performance on this dataset and outperforms other methods by a large margin.

The original CameraFusion (Wang et al. 2021) dataset contains 146 pairs of wide-angle and telephoto images (4k resolution). However, the two kinds of images are captured by lens switching, leading to different contents between the two cameras in dynamic scenes. Therefore, we first remove the pairs that the contents cannot be matched in the overlapped FoV area. Then, we utilize our alignment method to construct LR-HR-Ref triples. After removing the LR-HR pairs with large misalignments, only 98 triples are kept. Note that, compared with the other two datasets, there are still small misalignments in this dataset due to its lens switching based capturing method.

Considering the number of image triples in the above two datasets is still limited, we further construct our DuSR-Real dataset, which contains 420 training triples and 55 testing triples. Fig. 5 presents some examples of the HR images in our dataset, which cover multiple kinds of scenes. In ad-



Figure 5: Exemplars of the aligned HR images in our DuSR-Real dataset.

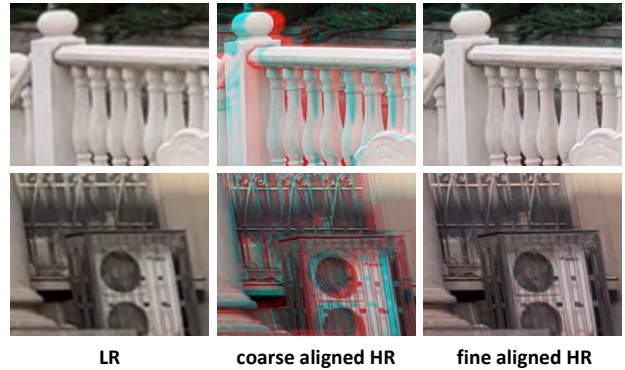


Figure 6: Illustration of LR-HR pairs in our dataset. From left to right: the LR input, the coarse aligned (SIFT based alignment) HR, and the fine aligned (deep flow based alignment) HR. The LR and fine aligned HR construct the LR-HR pairs in our dataset. To visualize the misalignments, we replace the red channel of the two kinds of HR by the red channel of the LR input. It can be observed that the coarse aligned HR has large displacements with the LR while the fine aligned HR is accurately aligned with the LR.

dition, the LR-HR pairs in our constructed dataset are accurately aligned. As stated in the main paper, we utilize a coarse to fine alignment strategy. Fig. 6 presents two examples of the input LR and its corresponding aligned HR. The first column is the input LR, namely the wide-angle image. The middle column is the coarse aligned HR. We replace its red channel by the red channel of the LR to visualize the misalignments between the two images. The right column is the HR after fine alignment. We also replace its red channel by that of the LR. It can be observed that after fine alignment, the LR and HR are well aligned, which constructs a suitable pair for supervised learning. Table 6 summarizes the three datasets. The image number and scene number in our dataset are the largest.

Dataset	Image Number (Training + Testing)	Scene Number (Training + Testing)	Scale Factor	HR Resolution
DuSR-Real	420 + 55	305 + 55	2	1792×896
RealMCVSR-Real	330 + 50	210 + 27	2	1792×896
CameraFusion-Real	83 + 15	65 + 15	2	3584×2560

Table 6: Comparison of the three datasets for real dual-lens SR.

Differences in Alignment for Dataset Construction and Center Warping

For dataset construction (center warping), we utilize DeepFlow (flow-guided DCN). DeepFlow is more accurate but is non-differentiable and much slower than DCN. Therefore, for dataset construction, we utilize the more accurate DeepFlow. By manually removing the cases that cannot be well aligned by DeepFlow, we generate a well-aligned dataset. For center warping, we utilize the faster and differentiable DCN.

	RCAN	SwinIR	ESRGAN	BSRGAN	TTSR	MASA	DATSR	DCSR	SelfDZSR	ZeDuSR	KeDuSR
Latency(s)	0.69	2.85	0.08	0.45	7.51	1.52	9.35	0.84	0.17	180	0.51
Params (M)	5.63	11.75	16.7	16.61	6.25	4.02	10.51	3.19	0.52	1.49	5.63

Table 7: Latency and Parameter.

Complexity Comparison.

We present the latency and number of parameters in Table 7. Our method ranks second among all the RefSR and the dual-lens SR methods in terms of latency. Latency indicates the time required to generate one HR result (1792×896) using one NVIDIA 3090 GPU.

Visual Comparisons with State-of-the-arts

Visual comparisons on DuSR-Real dataset. We further present more visual comparison results on DuSR-Real dataset. As introduced in the main paper, we compare with RCAN (Zhang et al. 2018b), TTSR (Yang et al. 2020), MASA (Lu et al. 2021), DCSR (Wang et al. 2021), SelfDZSR (Zhang et al. 2022b), and ZeDuSR (Xu, Yao, and Xiong 2023). Our approach demonstrates superior performance in both center and corner regions, as shown in Figs. 7.

Blocking artifacts. Both the RefSR and dual-len SR methods consume a substantial amount of GPU memory and we need to partition the LR input into blocks for processing, which may lead to blocking artifacts. In our implementation, we split the LR input into 128×128 patches with an overlap of 8 pixels. Except SelfDZSR and ZeDuSR, which consume small memory costs, all the other RefSR methods are split into patches in the same way. As shown in Fig. 8, TTSR, MASA, and DCSR introduce visible blocking artifacts. In contrast, our results have no blocking artifacts. The reason is that our approach utilizes kernel-free matching, which makes the brightness to be consistent across the whole image.

Visual comparisons with full-resolution inputs. In order to have ground truth, the DuSR-Real dataset we have utilized for evaluation is constructed by cropped images. To comprehensively evaluate the effectiveness of our approach on real-world data, we utilize the real captured original full-resolution wide-angle and telephoto images as inputs for comparison, as shown in Fig. 9. Note that, in this case, there is no ground truth. It can be observed that our method recovers the most vivid details for the center region.

Ablation Study Results

Visual comparisons. As demonstrated in the main paper, there are four variants in our main paper. Since variant A utilizes traditional matching, its center and corner SR results are both worse than our full-model (as shown in Fig. 10), namely variant D. For variant B, since there is no corner warping, its corner SR results are smooth. For variant C, since its center region is not well aligned, the center SR result is worse than our full model (D). Variant D achieves the best SR result in both center and corner regions.

Ablation on global warping. As stated in the main paper, the first step for center warping is utilizing SIFT matching to calculate the homography transformation matrix. In this way, we align I^{Ref} with I^{IR} globally (the global aligned Ref is \hat{I}^{Ref}), and identify the overlapped region I^{IRC} . We would like to demonstrate that our method is robust to this step. Since the two cameras have a fixed relative position, we can also utilize a fixed homography transformation for the global warping. As indicated in Table 8, ‘fixed’ employs a fixed homography matrix to align each image globally, while ‘adaptive’ indicates that each image is aligned using SIFT matching. The results demonstrate that even with ‘fixed’ global transformation, our method still generates promising results.

Global Warping	DuSR-Real
fixed	27.51 / 0.8830
adaptive	27.66 / 0.8890

Table 8: Ablation on the global warping method. The results are evaluated on our DuSR-Real dataset.

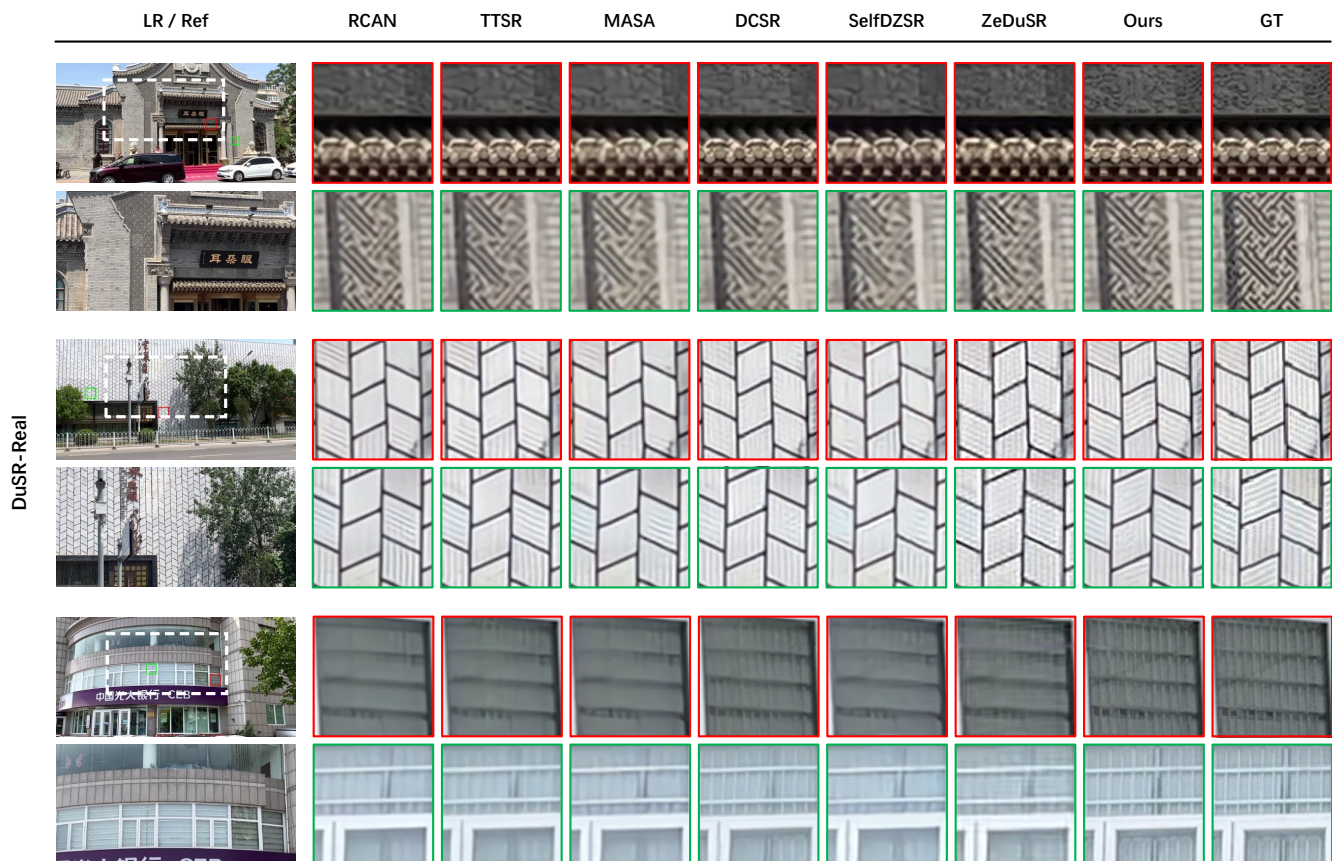


Figure 7: Visual comparisons on DuSR-Real dataset. The white dotted box indicates the overlapped FoV area between LR and Ref. The presented results are obtained with only reconstruction loss.

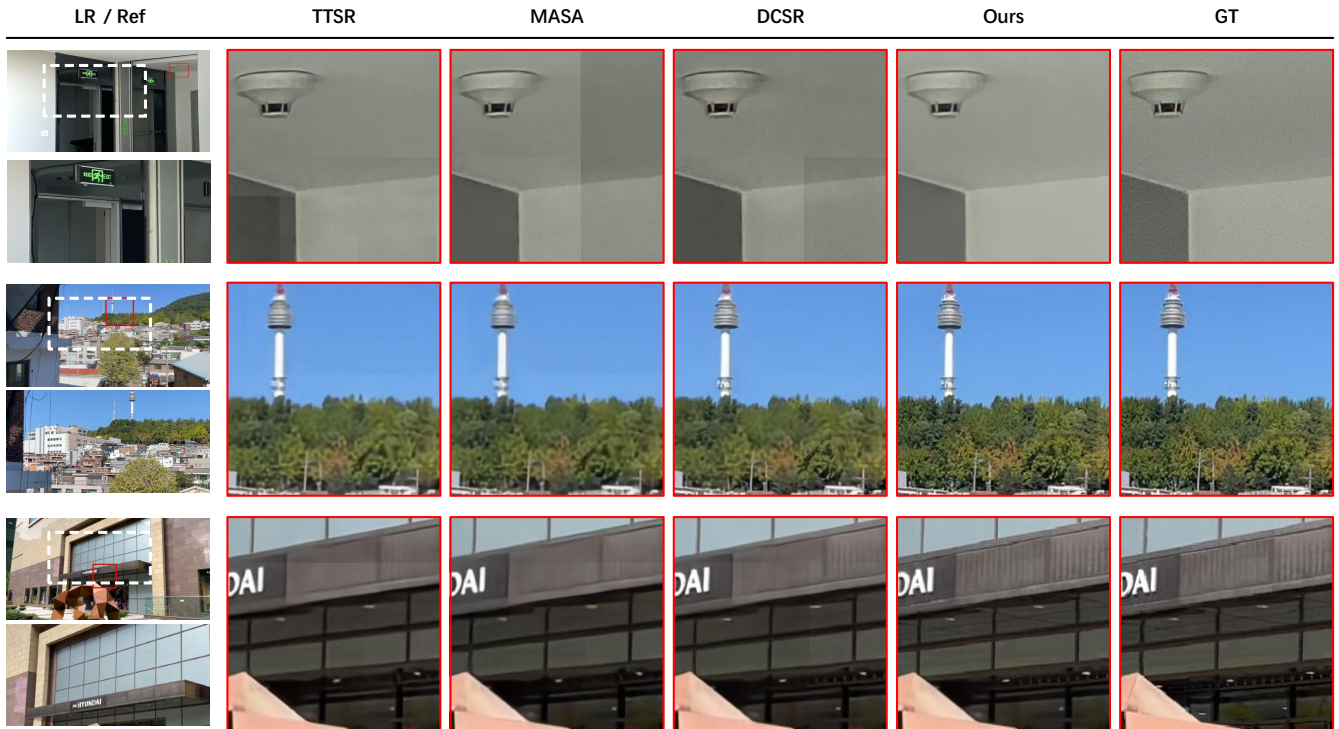


Figure 8: Visual comparisons about the blocking artifacts. The white dotted box indicates the overlapped FoV area between LR and Ref. The presented results are obtained with only reconstruction loss.



Figure 9: Visual comparisons on full-resolution inputs. The white dotted box indicates the overlapped FoV area between LR and Ref. The presented results are obtained with only reconstruction loss. Note that there is no ground truth in this case.

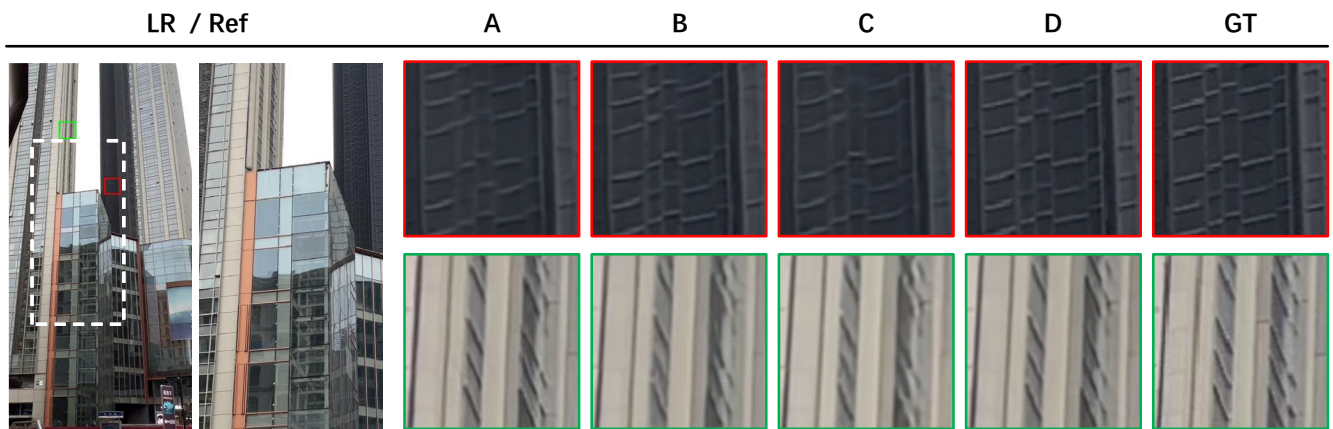


Figure 10: Visual comparisons of ablation study. The white dotted box indicates the overlapped FoV area between LR and Ref. The presented results are obtained with only reconstruction loss.